RSP-0288

TECHNICAL REPORT UOME-RBB-2012-04
(Grid spacer simulations)

Research Contract:	Canadian Nuclear Safety Commission, Contract 87055-11-0518
Project Title:	R522.lb - International CFD Benchmark Problem: Turbulent Flow in a Rod Bundle with Spacers
Task:	Final report
Principal Investigator:	S. Tavoularis, Professor Department of Mechanical Engineering
Investigator:	D.I. Chang, Research Associate
Date of Submission:	November 30, 2012

uOttawa

L'Université canadienne
Canada's university

Abstract

Numerical simulations of turbulent flows in a rod bundle with two types of spacer grids (split-vane type and swirl-vane type) have been performed within the framework of an international blind CFD benchmark exercise. Details of the test geometry and conditions were provided by the Korea Atomic Energy Research Institute (KAERI), South Korea. The model of the computational geometry was based on the provided CAD files, with some parts simplified in order to avoid deterioration of the mesh quality.

In the present analysis, we used the segregated turbulence model, consisting of a combination of SAS (Scale Adaptive Simulations, which are second generation solutions of the unsteady Reynolds-averaged Navier-Stokes equations) and LES (Large Eddy Simulations). This hybrid approach achieves the accuracy of LES at a computational cost that is lower than that of full LES. The simulations employed the second-order central difference scheme for the discretization of the convection terms of the transport equations, and the second-order implicit Euler scheme for temporal discretization. As inlet boundary condition for the velocity distribution, we used results of steady, separate simulations of flow in the bare rod bundle.

On May 8, 2012, our numerical results for the split-vane spacer grid, using 22M cells, and the swirl-vane spacer grid, using 20M cells, were submitted to the organizer (KAERI) in the form of time-averaged velocity and rms velocity fluctuation profiles in quadrant sections of planes located $0.5D_\mathrm{h}$, $1.0D_\mathrm{h}$, $4.0D_\mathrm{h}$, and $10.0D_\mathrm{h}$ downstream of the spacer grid tips. Contours of streamwise vorticity and circulation values on these planes were also provided.

KAERI received 21 submissions for the split-vane spacer grid case, and ranked our time-averaged velocity data at $z = 1.0D_\mathrm{h}$ in the 11th place and those at $z = 4.0D_\mathrm{h}$ in the 3rd place. KAERI received 14 submissions for the swirl-vane spacer grid case, and ranked our time-averaged velocity data at $z = 1.0D_\mathrm{h}$ in the 1st place and those at $z = 4.0D_\mathrm{h}$ in the 4th place. For the split-vane spacer configuration, fair agreement was obtained between the predicted lateral

and spanwise velocities and the experimental ones; however, the predicted streamwise velocity was far from the measured one. This difference is attributed to the low mesh quality. For the swirl-vane spacer configuration, the predicted velocity showed excellent agreement with the experimental data; however, the predicted turbulence stress values for both spacer grid simulations were significantly lower than the experimental results. This is attributed to the mesh in the downstream rod bundle zone being too coarse.

To improve the prediction of the turbulence level, we conducted a refined simulation of the split-vane spacer configuration, using 40M cells after refining the mesh of the 22M cell case in the downstream rod bundle zone. The simulation results were in good agreement with the experimental data. This indicates the importance of the mesh quality and mesh size, especially in the downstream rod bundle zones, where LES was applied.

Contents

1. Motivation and background

The majority of studies of flow and heat transfer in nuclear industry have been experimental, mostly using drastically simplified geometrical models under conditions that are far less complex than those in operating nuclear reactors. The measurement of the flow properties was in most cases restricted to several line traverses or measurements on a single plane. In this respect, Computational Fluid Dynamics (CFD) analysis offers a viable alternative to experimental testing and, when properly validated, can lead to improved design and maintenance in a relatively cost effective and timely manner. Although CFD have evolved significantly in the past decades with the growth of computing power and have been used as valuable tools for analyzing complex flow and heat transfer phenomena in various engineering fields, the accuracy of CFD results have been strongly dependent on many factors including turbulence models, mesh resolution, time step size, inlet boundary conditions, and numerical schemes. Tavoularis (2011) has recently raised a number of concerns that apply to CFD predictions and emphasized the importance of verification and validation to demonstrate the accuracy of CFD results. Validation of CFD predictions is to quantify the numerical accuracy by comparing with experimental results, which may only be appropriate if the corresponding geometries and conditions are the same. Therefore, the complete and accurate specification of geometrical data used in experimental studies is crucial for validation of CFD. In consequence of the fact that commercial spacer grid data are highly proprietary, numerical studies of the effect of such spacers in rod bundle flows have been rarely conducted, whereas there are many CFD studies of bare-rod bundle flows. Acknowledging the limited availability of the spacer grid data and the importance of CFD validation, the Committee on the Safety of Nuclear Installations (CSNI) of Nuclear Energy Agency (NEA), affiliated with the Organization for Economic Cooperation and Development (OECD), has organized one of WGAMA (Working Group on the Analysis and Management of Accidents) groups to launch a blind CFD benchmark exercise for the prediction of turbulent flow in a rod bundle with spacer grids. During the CFD benchmark period, CFD participants in this exercise have been given details of the test geometry and conditions of the rod bundle tests performed in the MATiS-H (Measurements & Analysis of Turbulence in Subchannels – Horizontal) facility of the Korea Atomic Energy Research Institute (KAERI) in Daejeon, South Korea.

This benchmark exercise was an opportunity to strengthen Canadian contributions towards establishing best practice guidelines for the use of CFD in nuclear reactors safety applications. The following sections summarize the objectives, the computational procedure and conditions, the mesh dependence analyses, and the results.

2. Objectives

The objective of the blind benchmark exercise was to conduct numerical simulations of single-phase isothermal turbulent water flow in the MATiS-H rod bundle with a spacer grid for two cases with different geometrical configurations of the spacers, and later to compare the predictions with measurements provided after the blind prediction submission deadline.

3. Computational procedures and conditions

3.1. Computational geometry

The geometry and conditions used in the present study were meant to reproduce the measured results in the MATiS-H experiments by KAERI researchers, who conducted LDA (laser Doppler anemometry) measurements in a 5 × 5 rod bundle array of the MATiS-H cold loop test facility to investigate the effects of two types of spacer grids (split-type spacer grid and swirl-type spacer grid) and to provide experimental data for the CFD benchmark exercise.

Figure 1 shows the cross-section of the 5 × 5 rod bundle array, inserted in a square duct. The entire cross section of the duct was included in the model rather than a section of it, as spatial periodicity of the flow cannot be assumed downstream of a mixing vane spacer grid. The duct cross-section has a side h = 170.0 mm. Each rod has an outer diameter D = 25.4 mm and the hydraulic diameter of the rod bundle cross-section is D_h = 24.3 mm. The rod and wall pitches are P = 33.1 mm and W = 18.8 mm, respectively, which correspond to a rod pitch-to-diameter ratio P/D = 1.3 and a wall pitch-to-diameter ratio W/D = 0.7.

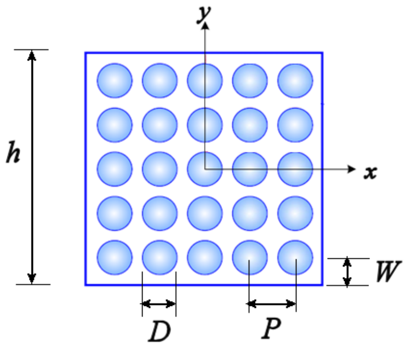

Figure 1. Cross-section of the 5 × 5 bare rod bundle array showing definitions of the height (*h*) of the square duct, rod diameter (*D*), pitch (*P*) and wall pitch (*W*).

Figure 2 shows the MATiS-H test rig, in which water flows from the inlet, located on the far right side of the figure, to the outlet, located on the far left side of the figure. The turbulent water flow in the rod bundle was under isothermal conditions, at a temperature of 35ºC, and was subjected to no gravitational effects. The density of water was taken as 994.06 kg/m^3 and its dynamic viscosity as 0.00072 kg/ms. The mass flow rate of water in the test rig was 24.2 kg/s and the bulk velocity was 1.5 m/s. The Reynolds number, based on the bulk velocity and the hydraulic diameter, was 50,250.

Except for a short upstream section, the test rig contained a rod bundle, which had a length of 3,863.0 mm (159D_h). A first flow straightener was positioned in the test rig upstream of the rod bundle, with the objective to produce a nearly uniform velocity across the duct. A second flow straightener was inserted in the section containing the rod bundle, at a distance 100D_h upstream of the spacer grid (S/G), which KAERI considered to be long enough for the flow to be expected to be fully developed at the entrance to the S/G. Velocity measurements in the rod bundle flow was only possible at cross section A-A´, which was located 5.0 mm upstream of the downstream end of the rod bundle. They could be taken from either of two acrylic windows, one located on the side of the rod bundle (parallel to the flow direction) and another located at the outlet tank (perpendicular to the flow direction). The measuring system was a two-dimensional laser-Doppler anemometer (LDA).

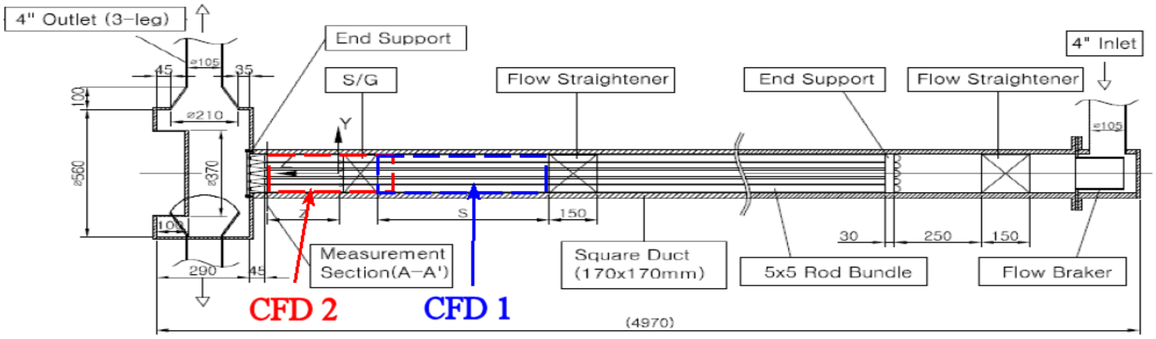

Figure 2. Side view of the MATiS-H test rig (OECD/NEA, 2012).

The CFD model did not include the entire MATiS-H test rig but a part of it because the former requires excessive computational resources (RAM memory) to build a proper mesh. Figure 2 shows two CFD zones in the test rig. The CFD1 zone included the bare-rod bundle, while the CFD2 zone included a rod bundle with a spacer grid.

The detailed spacer grid strap, not including vanes, is shown in Fig. 3. Each square channel contained 4 × 2 buttons to support each rod in the right position. The distance between the upstream button layers and the downstream button layers was $3.29D_h$. The length of the spacer grid was $4.24D_h$.

Figure 4 shows the two tested types of mixing vane configurations. The split-vane spacer grid had two vanes at every cross section of the grid strap, whereas the swirl-vane spacer grid had four vanes. A vane was oriented at an angle of 30 degrees relative to the streamwise direction (OECD/NEA, 2012). CAD files of both mixing vane spacer grid geometries were provided to ensure an accurate CFD model generation.

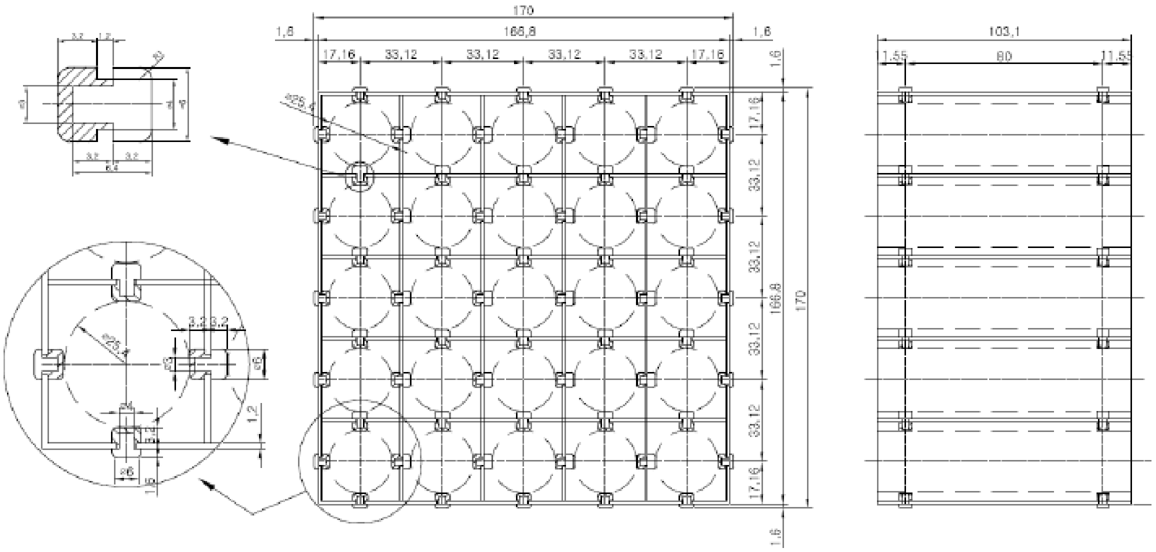

Figure 3. Strap and button details in the spacer grid: digits in mm (OECD/NEA, 2012).

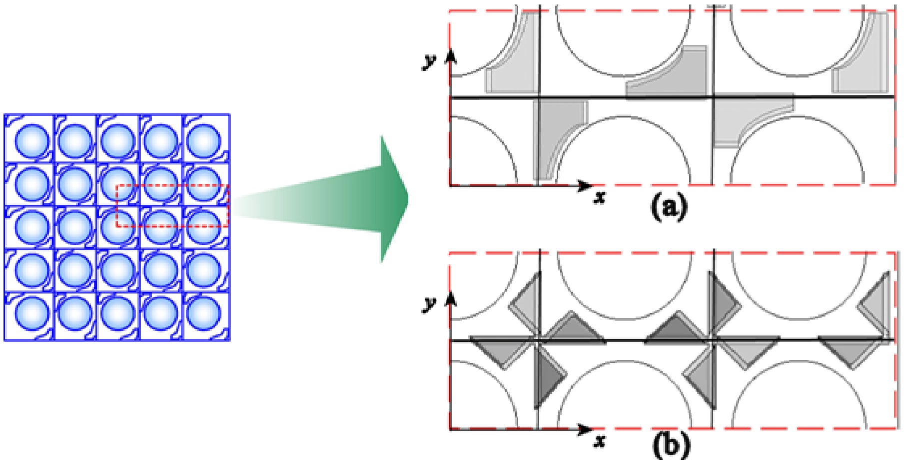

Figure 4. Spacer grids tested in the MATiS-H test rig: (a) split-vane spacer grid, (b) swirl-vane spacer grid.

The vane lengths for the split-vane type and swirl-vane type were, respectively, 16.90 mm ($0.70D_h$) and 17.93 mm ($0.74D_h$). Despite this slight difference ($0.04D_h$) between the lengths of two vane types, the lengths of the computational sub-domains for both types of vanes were kept the same and equal to $0.9D_h$. Therefore, the computational geometry in Fig. 5 represented both vane types. The length of the entire domain was approximately $27.1D_h$; it was the sum of i) the length of the upstream bare-rod bundle domain between the inlet plane and the mixing vane spacer grid ($10.0D_h$), ii) the mixing vane spacer grid length ($5.1D_h$), iii) the length of the downstream bare-rod bundle ($12.0D_h$). The mixing vane spacer grid was the sum of the length of the spacer grid ($4.2D_h$) and the length of the vane zone ($0.9D_h$). The downstream bare-rod bundle length was equal to the sum of the maximum distance between the downstream face of the spacer grid and the measurement plane ($10.0D_h$) and an additional length ($2.0D_h$) inserted to eliminate outlet effects on the simulation results. The four measurement planes were, respectively, located at distances 0.5, 1.0, 4.0 and $10.0D_h$ from the downstream face of the spacer grid. The origin of the Cartesian coordinate system was located at the center of the cross-section on the downstream face of the spacer grid, with the axes x, y and z, respectively, pointing toward the spanwise, transverse (normal to the bottom wall) and streamwise directions.

Although geometric modeling was based on the provided CAD files for the two types of spacer grids, parts of the computational geometry (grid buttons of the spacer grid strap and cavities in the swirl-vanes) were simplified in order to avoid deterioration of the quality of mesh, which would otherwise include highly skewed, small cells.

Figure 6 shows the end view of the rod bundle channel, which contained the split-vanes and grid buttons. The grid buttons were marked by dashed rectangles in red colour. Figure 6(a) is a CAD drawing; one may observe a narrow gap between the curved rod and the straight bottom surface of a grid button. Figure 6(b) shows our CFD geometry, in which the shapes of the grid button sides were changed to match the rod surface profile. The simplified grid buttons in the spacer grid strap were also used in the swirl-vane case.

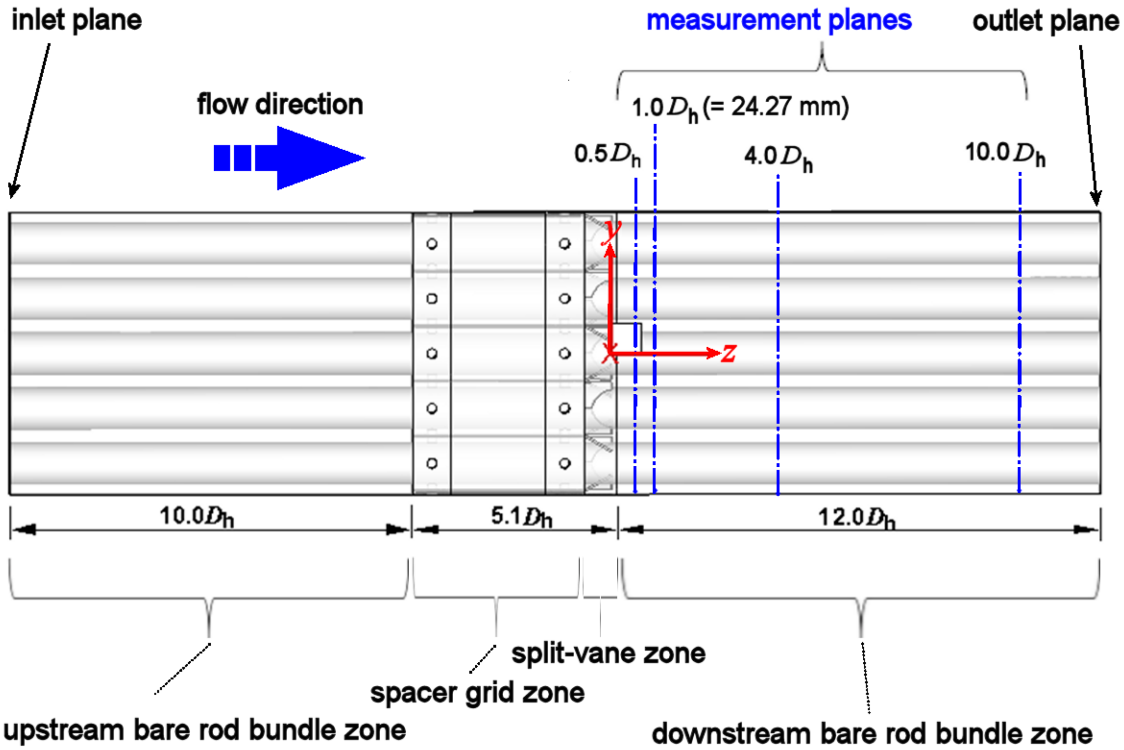

Figure 5. CFD model for the rod bundle array with a spacer grid.

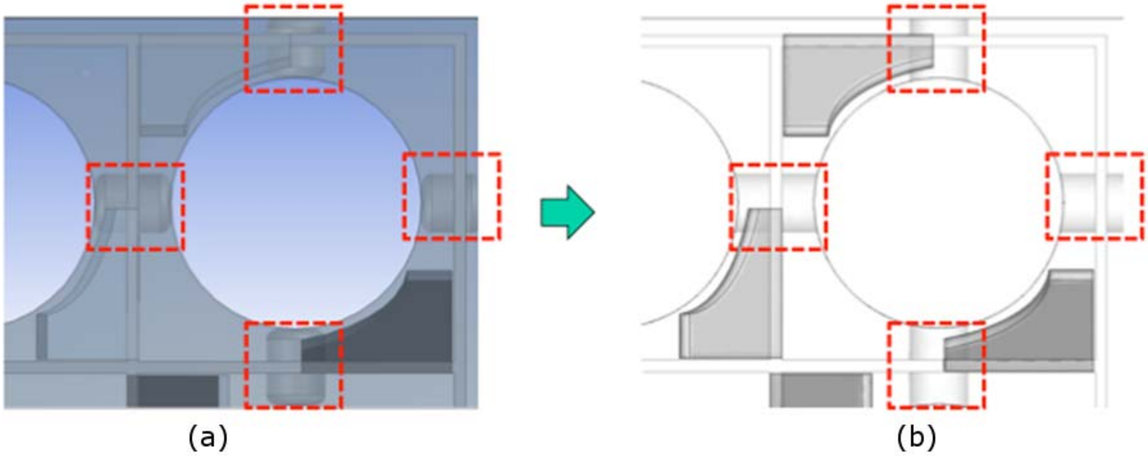
(a)
(b)

Figure 6. Sketches of (a) original and (b) simplified grid buttons.

Figure 7 shows the presence of cavities in the swirl-vanes, marked by red boxes. We filled up these cavities to avoid the need for highly skewed, small elements, which would cause mesh quality to deteriorate.

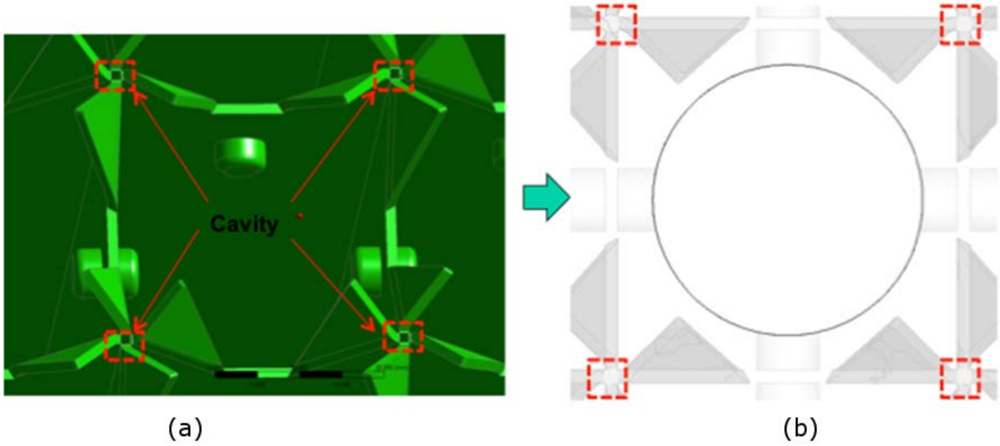

(a)
(b)

Figure 7. Sketches of (a) original and (b) filled cavities of swirl-vanes attached to the end of the spacer grid.

3.2. Mesh generation

Figure 8 shows the unstructured hybrid mesh used for the upstream and downstream rod bundle zones; it was composed of hexahedral elements in the sub-channel core regions and prismatic elements in the boundary layer regions. One of the primary concerns was how to cluster the grid points near the wall to resolve the steep velocity gradients in the boundary layer regions when turbulence models were integrated through the viscous sub-layers. 20 prismatic elements were allocated in the boundary layer region. The mesh was first distributed on the inlet and then was mirrored over the length of the domain toward the outlet so that the mesh distributions on all cross-sections were kept the same.

Figure 9 shows mesh distributions on the sidewalls of the rod bundle with a split-type spacer grid. The detail view shows that the tetrahedral mesh was used in the two grid button sub-domains and the vane sub-domain, while the hexahedral mesh was applied in the upstream and downstream rod bundle domains as well as in the middle section of the spacer grid. Geometric complexity with grid buttons and mixing vanes led us to choose the tetrahedral mesh rather than the hexahedral mesh, because the latter decreases the mesh quality. The streamwise spacing of the hexahedral mesh in the middle spacer grid zone between two grid buttons was kept the same as the one in the downstream rod bundle, in an effort to resolve properly vortex shedding from grid buttons and swirling flows induced by the mixing-vanes.

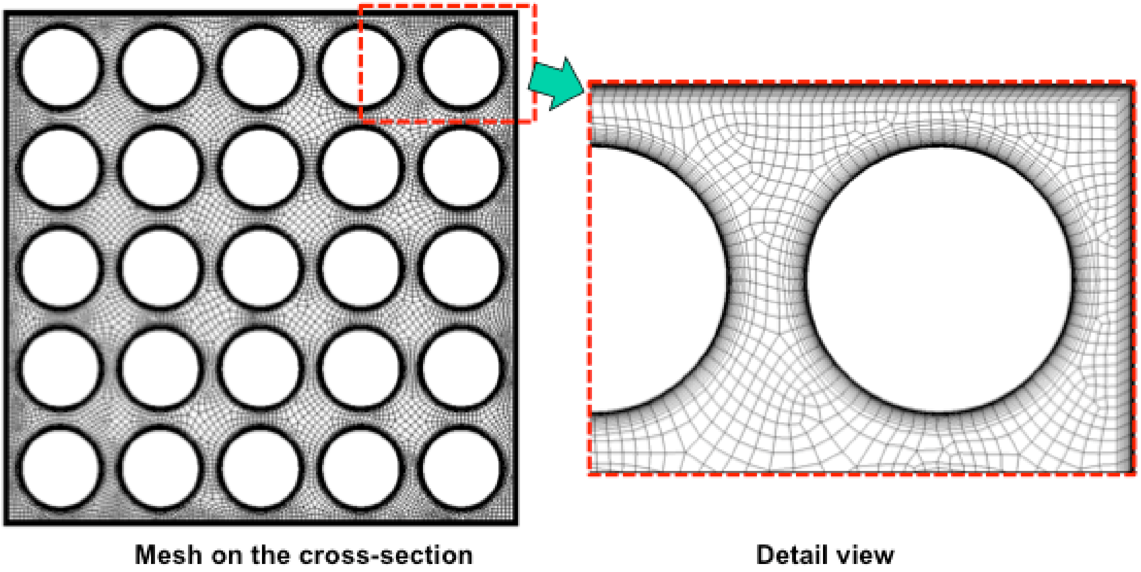

Figure 8. Unstructured hexahedral mesh in the bare rod bundle.

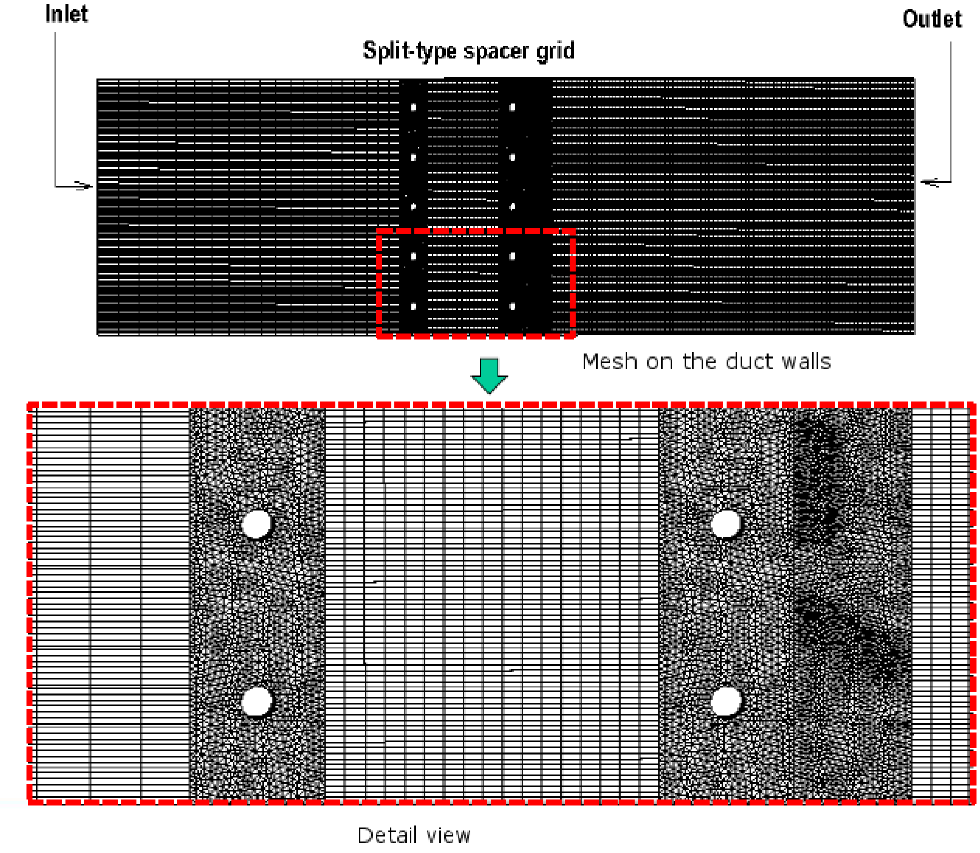

Figure 9. Unstructured mesh in the rod bundle with a mixing-vane spacer grid.

3.3. Numerical schemes

The simulations employed the second-order central difference scheme for the convection terms of the transport equations. The second-order implicit Euler scheme was employed for temporal discretization.

To avoid numerical instability caused by the combination of high-aspect ratio grid cells and highly-clustered near-wall spacing, as required for turbulence modelling, the SIMPLEC (Semi-Implicit Pressure Linked Equations – Consistent) algorithm was used for the treatment of pressure-velocity coupling.

All simulations have been conducted using the commercial package ANSYS Fluent 13.

3.4. Turbulence models

Before discussing the turbulence model for the present simulations, it is important to discuss available turbulence models and their resource requirements for the present flow, in which Re = 50,250. Direct Numerical Simulation (DNS) is the most accurate CFD method, but it requires extremely large computational resources and long computing time (fine mesh, small time step, and high-order discretization schemes) to resolve turbulent motions at scales comparable to the Kolmogorov microscale. The number of mesh cells for DNS is proportional to $Re^{2.25}$. This means that DNS would need a mesh with a number of cells elements of the order of 10^{10}, which is untenable. The next most accurate approach is Large Eddy Simulations (LES). LES solves low-pass filtered dynamic equations but it does not resolve sub-grid scale (SGS) motions, which are modelled with the use of a SGS model. Chapman (1979) showed that the number of cells needed for LES to resolve the viscous sublayer is proportional to $Re^{1.8}$. LES would require a mesh with a number of cell elements of the order of 10^8. Furthermore, it is highly plausible that this number would need to increase to accommodate complex geometric features (mixing vanes, grid strap, grid buttons, and subchannel walls). As means to avoid the large mesh size needed in DNS and LES, several hybrid methods have been introduced. In the segregated hybrid method, LES is applied in a small sub-domain where large-scale turbulence structures are resolved and URANS is applied in a large sub-domain where all turbulence scales are modelled. This hybrid approach can maintain the accuracy of LES at a lower computational cost (Chang and Tavoularis, 2012a). In the present analysis, we chose to simulate the flows in the rod bundle with spacer grids using the segregated-hybrid type method, consisting of a combination of SAS (Scale Adaptive Simulation; second generation URANS) and LES.

The computational domain was divided into two sub-domains, as shown in Fig. 10. SAS was used in the upstream rod-bundle sub-domain and the spacer grid sub-domains, whereas LES was used in the mixing vane sub-domain and the downstream rod-bundle sub-domain. The SAS introduces source terms in the ω equation in terms of the von Kármán length scale, which is the ratio of the first and the second velocity gradients. The SAS acts like LES in detached flow regions where the von Kármán length scale is relatively small, while it works as URANS in the stable flow regions without separation where the von Kármán length scale is increased. In this work the shear stress transport (SST) model (Menter, 1991) was chosen as the turbulence model for the URANS. The SAS model can resolve scales without grid information as it contains no explicit term specifying the grid spacing. Details have been provided by Menter and Egorov (2005).

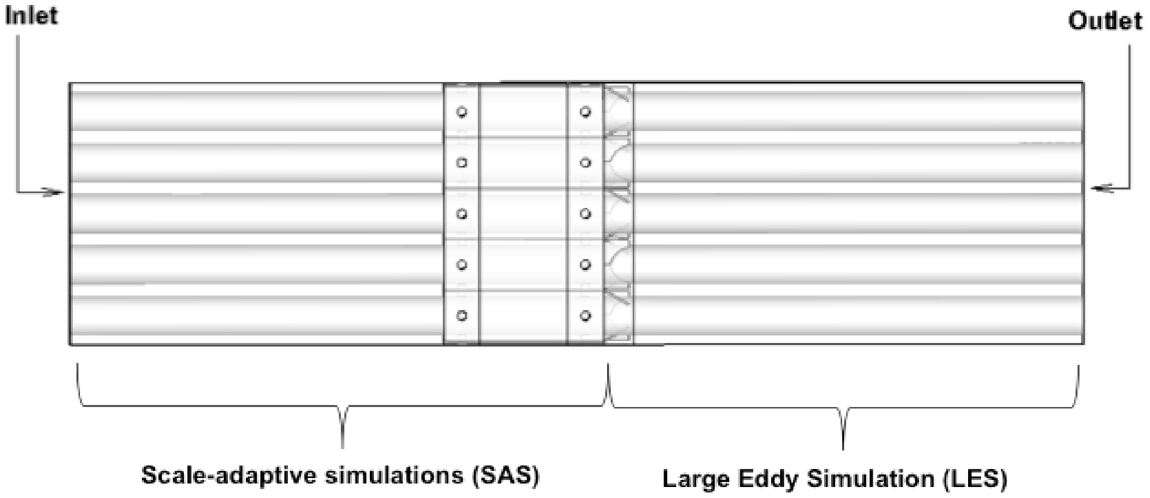

Figure 10. Assignment of hybrid turbulence models in the different computational sub-domains.

The wall-adapting local eddy-viscosity (WALE) model (Nicoud and Ducros, 1999) was chosen as a subgrid model for the LES because this subgrid model is capable of predicting correctly the asymptotic flow behaviour near the wall in wall-bounded turbulent flows, due to its use of the square of the velocity gradient tensor (Wornom *et al*. 2011).

3.5. Boundary conditions

In the interface between the SAS and the LES and in the inlet plane, the velocity fluctuations were modeled by using the synthetic eddy method (SEM – also called the vortex method) to specify time-varying velocity fluctuations. The SEM, proposed by Sergent (2002), adopts a particle discretization method to solve the two-dimensional evolution equation of the vorticity for the lateral fluctuations and solves an one-dimensional Langevin equation for the streamwise fluctuations. No-slip conditions were applied at all walls. KAERI released measured data tables, which were meant to serve as an inlet boundary condition for the numerical simulations of rod bundle arrays with spacer grids. However, these measurements were restricted to those parts of the sub-channels that were optically accessible from outside the duct and were not sufficient for use as an inlet boundary condition in CFD analyses. In the inlet plane, the velocity was specified as discussed in the next section. The outflow boundary condition was imposed at the outlet, which extrapolates the data inside the computational domain by assuming a zero diffusion flux.

3.6. Inlet velocity specification

To generate a velocity distribution in the entire inlet, we conducted separate simulations of the bare-rod bundle. For validation purposes, the bare-rod bundle predictions have been compared with corresponding measurements that were released by KAERI in the final benchmark specification.

The entire cross-section of the bare rod bundle was modelled, rather than assuming flow symmetry. The geometric model for the bare-rod bundle simulations covered the zone downstream of the second flow straightener. The length of the computational domain was 2305.65 mm ($95D_h$), which was approximately 5% longer than the specified distance of 2184.3 mm ($90D_h$) between the flow straightener and the measurement plane, in order to eliminate possible sensitivity of the simulation results to outlet effects. The mesh in the bare rod bundle had 2.9 million cells.

Because the computational domain for the bare-rod bundle simulations covered the zone downstream of the second flow straightener, the velocity distribution at the inlet of the rod bundle should ideally be taken to be the one at the exit of this flow straightener. However, KAERI provided no relevant measurements, but instead speculated that the flow at the exit of the second flow straightener would be uniform, without giving any evidence to support this statement. On the contrary, a review of previous literature on flow management devices indicates that such honeycomb-like devices would be effective in straightening the flow, for example by removing large-scale streamwise swirl or vortex streets that may be present near narrow gaps, but would not eliminate velocity non-uniformities. In the absence of any usable information, we had no choice but to impose a uniform inlet velocity profile for the bare rod bundle simulations. We further imposed the outflow boundary condition at the outlet.

The Reynolds stress model (RSM) was chosen instead of simpler and faster two-equation models (e.g., the k-ε model), because the latter cannot resolve the strong turbulence anisotropy in gap regions and secondary flows in the corners of the square duct. The simulations employed the second-order upwind scheme for the convection terms of the transport equations.

Figure 11 shows experimental (left) and predicted (right) streamwise velocity contours on a quadrant of the cross-section at $z = 90D_h$. As noted previously, the measurements were restricted to optically accessible strips. The two sets of contours were comparable in the open channels, but agreement deteriorated toward the square duct walls. It is noted that the measurement uncertainty was higher in wall regions.

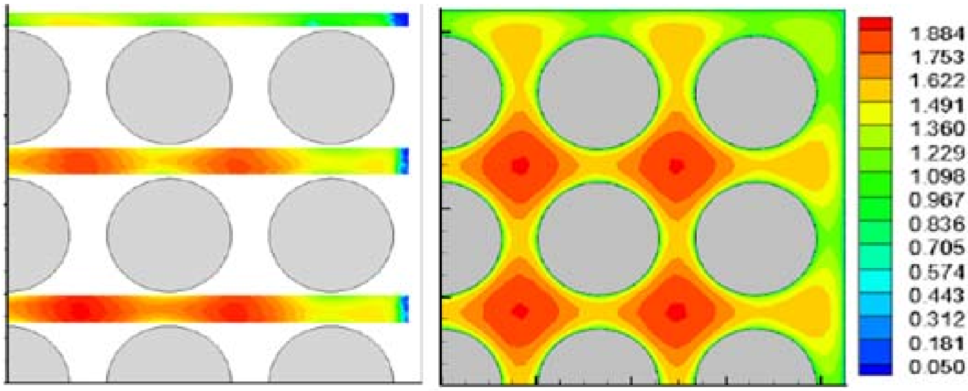

(a) (b)

Figure 11. Isocontours of the time-averaged streamwise velocity V_z (in m/s) at $z = 90D_h$: (a) KAERI experiments, (b) bare-rod bundle simulations using RANS with RSM.

Figure 12 shows predicted and measured spanwise profiles of the streamwise mean velocity and rms fluctuations at three traverse locations with y/P = 0.500, 1.500, and 2.455. As mentioned previously, the agreement between predictions and measurements was fairly good, except near the duct wall.

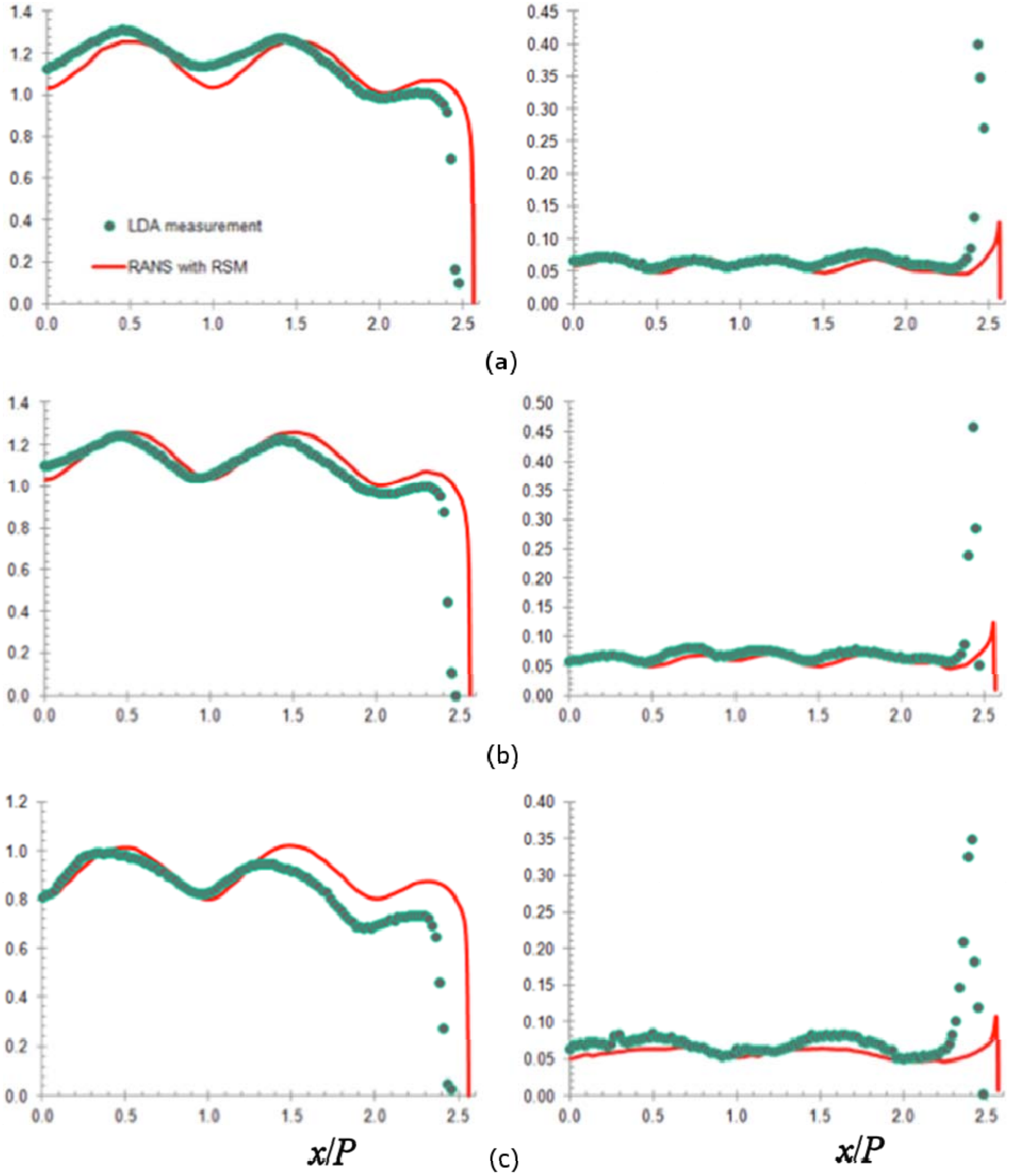

Figure 12. Spanwise profiles of the time-averaged dimensionless streamwise velocity V_z/V_b (left column) and rms streamwise fluctuations $V`_z/V_b$ (right column) at z/D_h = 90; y/P = 0.500 (a), 1.500 (b), and 2.455 (c).

Meyer (2010) and Chang and Tavoularis (2012a) suggested that time-resolving simulations (DNS, LES, URANS) should be used for tightly-packed rod bundles with $P/D < 1.2$ to resolve unsteady cross-flows in gap regions. Although the P/D value of the MATiS-H rod bundle is larger than 1.2, it seemed necessary to check whether the unsteadiness in the rod bundle can be ignored. To examine this, URANS simulations have been conducted for the same bare-rod bundle configuration. Figure 13 shows time histories of the cross-gap velocity at the wall gap centre for the two streamwise locations $z = 60D_h$ and $90D_h$. There was no evidence of cross-flow oscillations, and for all practical purposes the flow was steady. This supported our conclusion that unsteady RANS simulations were not necessary for the bare-rod bundle case.

The predicted velocity distributions at $z = 90D_h$ from the bare-rod bundle simulations using RANS were imposed in the inlet plane of the hybrid simulations for the split-vane and swirl-vane spacer grid cases. The turbulence intensity in the inlet plane was specified as 5%.

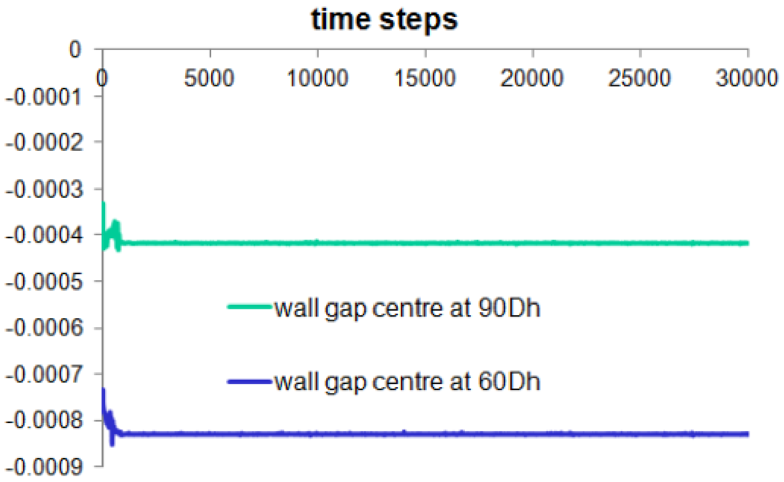

Figure 13. Time histories of the dimensionless spanwise velocity V_x/V_b at the wall gap centre at $x/P = 0$ and $y/P = 2.476$.

4. Mesh dependence analyses

In this section, two mesh dependence analyses will be presented: one using steady RANS simulations and second one using hybrid simulations.

4.1. Mesh dependence analysis using steady RANS

For a first mesh dependence analysis, RANS (Reynolds-averaged Navier-Stokes equation) simulations were employed because of their smaller computational resource requirement and shorter computing times, when compared to unsteady simulations. Four meshes were generated, containing 7M, 11M, 13M and 19M cells, respectively. The split-type spacer configuration was chosen in this mesh dependence analysis. Table 1 shows the mesh size of each sub-domain for these four cases.

Table 1. Meshes of the split-type spacer configuration used for the mesh dependence analysis using RANS

total mesh (number of cells)	mesh in upstream R/B zone	mesh in spacer grid zone	mesh in split-vane zone	mesh in downstream R/B zone
7.1M	0.5M	3.6M	2.5M	0.5M
11.4M	0.5M	3.6M	4.0M	3.3M
13.0M	0.5M	3.6M	5.6M	3.3M
19.1M	0.7M	9.5M	5.6M	3.3M

The RANS simulations used the RNG (Renormalization Group) k-ε model (Yakhot and Orszag, 1986) for turbulence modelling because of its robustness (i.e., numerical stability). The second-order upwind difference scheme was chosen for the spatial convection terms in the transport equations.

Figure 14 shows spanwise profiles of streamwise velocity and turbulent kinetic energy at $z = 1D_\mathrm{h}$ and $y = 0.5P$. It is evident that the solution converged as the mesh size increased. Although there was fair agreement between the results for the 13M and 19M cell cases, it was decided to use 19M cells as the standard mesh for the split-vane spacer grid simulations.

Figure 15 shows the numbers of mesh elements that were generated in the different sub-domains for the split-vane spacer grid geometry. The entire computational domain had a total of 19.1 million cells; the split-vane sub-domain had 29% of the total; each of the front and aft grid-button sub-domains had 21% of the cells; and the middle spacer grid sub-domain between two grid buttons had 6% of the cells.

A total of 20.6 million cells were generated for the entire computational domain of the swirl-type spacer configuration; the swirl-vane sub-domain had 35% of the total; each of the front and aft grid-button sub-domains had 20% of the cells; and the middle spacer grid sub-domain between two grid buttons had 5% of the total cells.

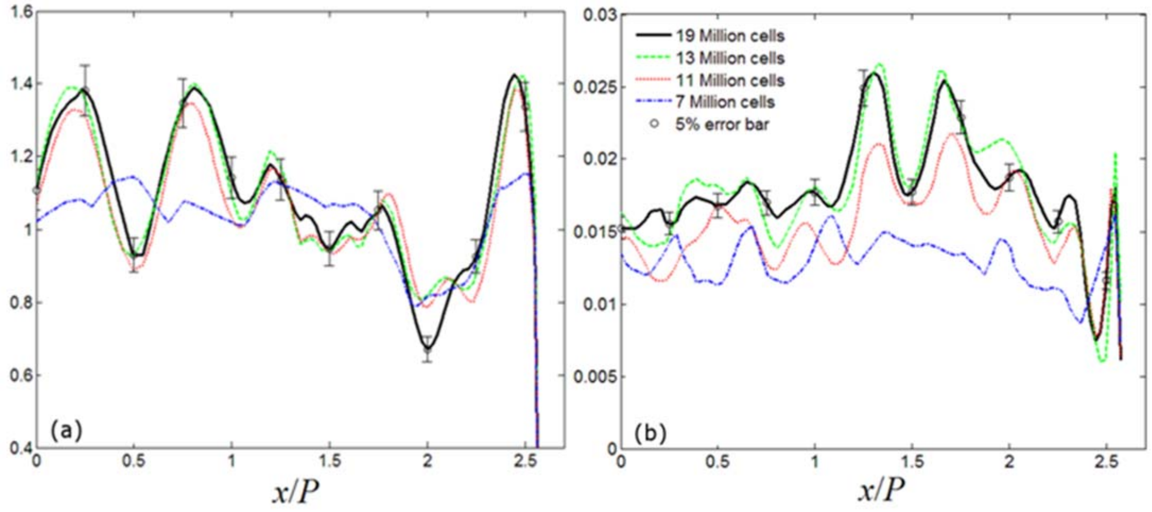

Figure 14. Effect of mesh resolutions on spanwise profiles of the dimensionless streamwise velocity V_x/V_b (a) and dimensionless turbulent kinetic energy $k/(V_b)^2$ (b) at $z = 1D_h$ and $y = 0.5P$.

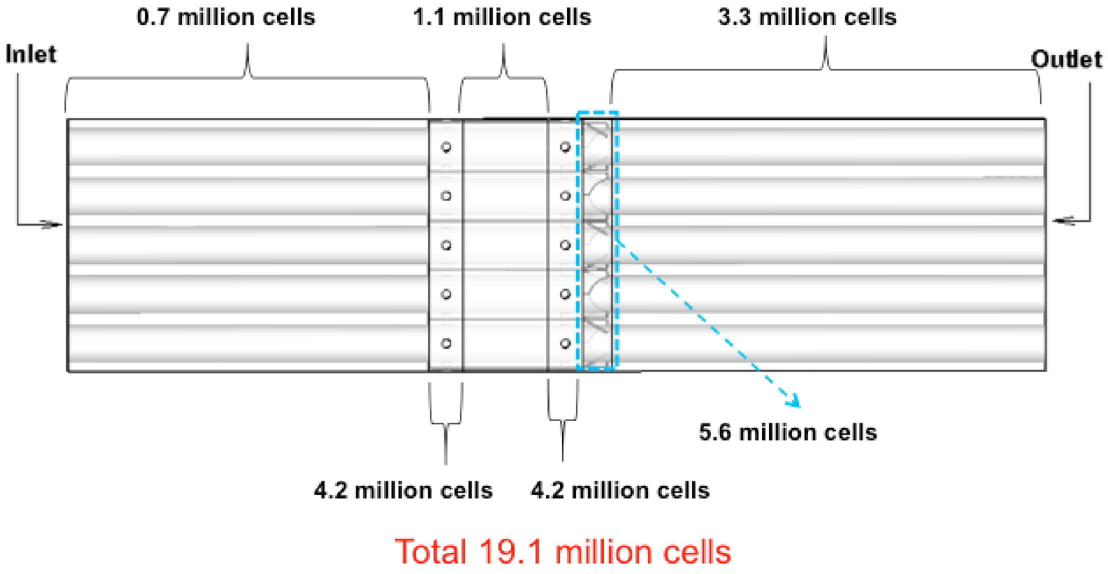

Figure 15. Mesh elements in each sub-domain for the split-type spacer grid.

4.2. Mesh dependence analysis using hybrid simulations

In the previous section, RANS simulations were employed for the mesh dependence analysis as verification. However, because the hybrid method was used for the main simulations, it is important to demonstrate that the meshes in LES zones were fine enough to resolve small-scale turbulent motions. Three meshes for the split-vane spacer grid configuration were generated, containing 19M, 22M, and 40M cell elements, respectively. Table 2 shows the number of cell elements for each sub-domain as well as the total one. The 22M cell case was generated after refining the mesh of the 19M cell case in the spanwise and transverse directions, but not in the streamwise direction. The 40M cell mesh was obtained after refining the mesh of the 22M cells in the streamwise direction and adding some more cells in the spanwise and transverse directions to the mesh of the 22M cell case.

Figure 16 shows profiles of the streamwise velocity V_z/V_b (Fig. 16a) and rms spanwise fluctuation V'_x/V_b (Fig. 16b) at $z = 1D_h$ and $y = 0.5P$. The streamwise velocity profile of the 22M cell case is different from those of the 19M and 40M cell cases. This difference is attributed to the low mesh quality of the 22M cell case as the mesh of the 19M cell case was refined in the spanwise and transverse directions. Figure 16 (b) shows that the predicted spanwise rms velocity fluctuations increased with mesh refinement.

The computing times for each hybrid simulation are listed in Table 3. The computing time was the sum of the solution developing time and the data collecting time for time averaging. One may note that the differences among the computing times for the three cases were not significant; compared to the 19M cell case, the 22M cell case required 1% more computing time, whereas the 40M case needed 5% more. One must, however, take into consideration that the 19M cell case was started from a specified initial state, whereas the two larger cases were started using the solution of the 19M cell case, which resulted in significant savings in computing time. All simulations were conducted on 64-bit Linux servers with 6 Quad core 6234 processors operating at 2.4 GHz and with 64 GB RAM. 47 threads of CPU processors were used for the computations.

Table 2. Meshes used for the mesh dependence analyses using hybrid simulations.

total mesh (number of cells)	mesh in upstream R/B zone	mesh in spacer grid zone	mesh in split-vane zone	mesh in downstream R/B zone
19.1M	0.7M	9.5M	5.6M	3.3M
22.2M	0.7M	9.5M	5.6M	6.4M
40.1M	0.7M	9.5M	5.6M	24.3M

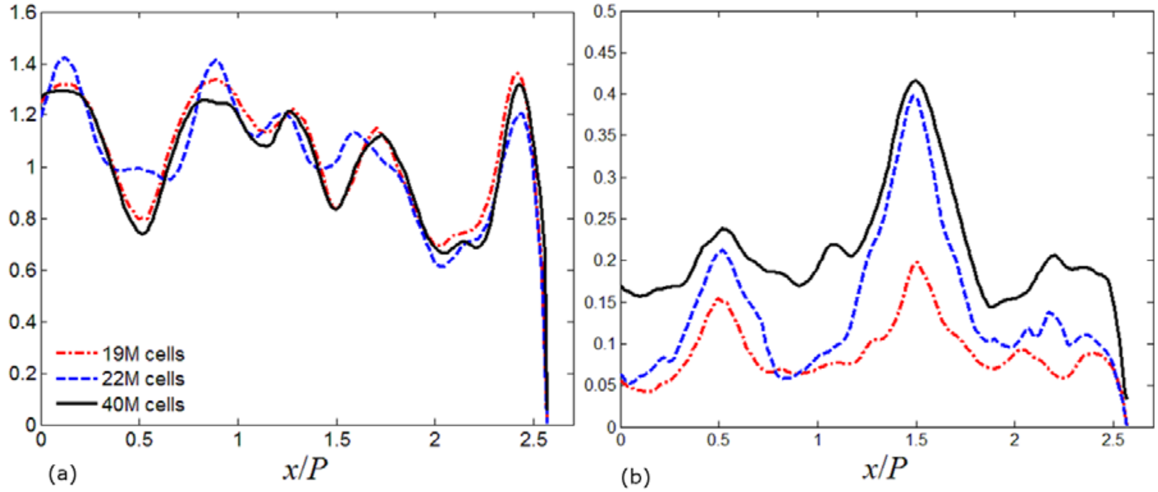

Figure 16. Spanwise profiles of (a) the dimensionless streamwise velocity V_z/V_b, (b) the dimensionless rms spanwise velocity fluctuation V'_x/V_b at $z = 1D_h$ and $y = 0.5P$.

Table 3. Computing times for hybrid simulations.

Case	Computing time (hours)
19.1M	2436
22.2M	2463
40.1M	2560

5. Blind CFD benchmark submission results

5.1. Canadian benchmark data

Szymanski *et al*. (2012) summarized the participation of the three Canadian teams, Atomic Energy of Canada Limited (AECL), McMaster University, and the University of Ottawa, in the blind CFD benchmark. Each team employed a different CFD approach, including choice of turbulence model, and spatial and temporal discretization schemes. The details are seen in Table 4.

Table 4. Specifications of Canadian team CFD approaches (Szymanski *et al*., 2012)

Organization	Code	Turbulence model	Mesh size (million)	Convective term scheme	Time-marching scheme	Computer resources	CPU time (hrs)
McMaster University	STAR-CCM+	RANS – RKE	63	2nd order upwind	Steady-state	32 CPU cluster	32
AECL	ANSYS Fluent 6.3.26	URANS – RSM	15.3	1st order upwind	1st order implicit	HP Z800 (6 cores)	336
University of Ottawa	ANSYS Fluent 13	Hybrid SAS/ LES	22.2	2nd order central	2nd order implicit	6 CPU server (48 threads)	2463

McMaster University conducted steady simulations, whereas AECL and the University of Ottawa conducted unsteady simulations. It is obvious that RANS simulations needed by far the shortest computing time and that the hybrid simulation required the longest computing time, because of the larger mesh size, higher order numerical schemes and more computationally expensive turbulence model, compared to the URANS study.

Szymanski *et al*. (2012) compared predictions of the time-averaged streamwise velocity, spanwise rms velocity fluctuation, and transverse rms velocity fluctuations. They found significant differences, especially for the rms velocity fluctuations. The hybrid simulations predicted the highest turbulence level, whereas URANS had the smallest one. Turbulence stress values in all three Canadian simulations were significantly lower than the experimental results as well as the refined-mesh hybrid simulations conducted by the University of Ottawa team after the benchmark submission.

5.2. Benchmark submission and results

On May 8, 2012, the numerical results for the split-vane and swirl-vane spacer grid cases were submitted to the organizer (KAERI) in the form of time-averaged velocity and rms velocity fluctuation profiles at y/P =0.500, 1.500, and 2.455 on a quadrant section of each measurement plane located at $0.5D_h$, $1.0D_h$, $4.0D_h$, and $10.0D_h$ downstream of the spacer grid tips, as shown in Fig. 17. Contours of streamwise vorticity and the circulation data in the blue dashed box were also provided in a separate text file.

KAERI received predictions from 25 participants from 12 countries by the extended deadline of May 28, 2012. KAERI compared the submitted results with experimental data and then ranked the data based on the velocity distributions at $y = 0.5P$ for two streamwise locations of $1.0D_h$ and $4.0D_h$. KAERI's ranking approach was questionable, because it did not consider velocity fluctuation data for the evaluation. This was pointed out by those who attended the synthesis presentation, at the CFD4NRS-4 workshop in Daejon, South Korea on September 10-12, 2012. Details about the ranking method and results are given in a workshop paper by Lee *et al*., (2012).

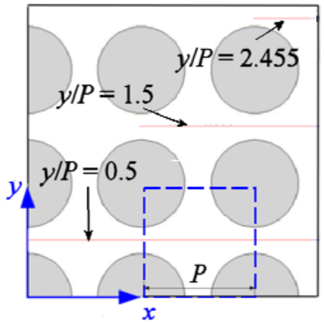

Figure 17. A quadrant section of a bare-rod bundle array; blue dashed box for streamwise vorticity contours; light red lines at y = 0.5P, 1.5P, and 2.455P for the plot results; this view is looking upstream.

5.2.1. Split-vane spacer grid simulations

KAERI received 21 submissions for the split-vane spacer grid case, including our submission with the 22M cell mesh. Our time-averaged velocity data were ranked at the 11th place for $z = 1.0D_\mathrm{h}$ and the third place for $z = 4.0D_\mathrm{h}$.

Figure 18 compares the time-averaged velocity predictions with the experimental data at $y = 0.5P$ for $z = 1.0D_\mathrm{h}$ and $4.0D_\mathrm{h}$. As the fluid moved downstream, the streamwise vortices lost their strengths and velocity peak variations decreased. Our simulations with 22M cells were in fair agreement with the experimental data for the spanwise and transverse velocities; however, they failed to follow the trend of the measured streamwise velocity. This is attributed to the low mesh quality of the 22M cell case.

Figure 19 shows the rms velocity fluctuation profiles at $y = 0.5P$ for $z = 1.0D_\mathrm{h}$ and $4.0D_\mathrm{h}$. At $z = 1.0D_\mathrm{h}$, the simulations generally underpredicted the turbulence levels except at the strongest peaks of the spanwise rms fluctuations (Fig. 19a) and transverse rms fluctuations (Fig. 19b). As discussed in section 4.2, the underprediction of the turbulence level indicates that the first mesh refinement in the spanwise and transverse directions was not fine enough to resolve turbulence properly in the downstream rod bundle zone. Therefore, a further refined hybrid simulation was conducted, in which the mesh of the 22M cell case was refined in the streamwise direction in the downstream rod bundle zone. Details of this refined hybrid simulation will be discussed in Chapter 6. At $z = 4.0D_\mathrm{h}$, agreement in overall turbulence levels between the prediction and the measurement was fair.

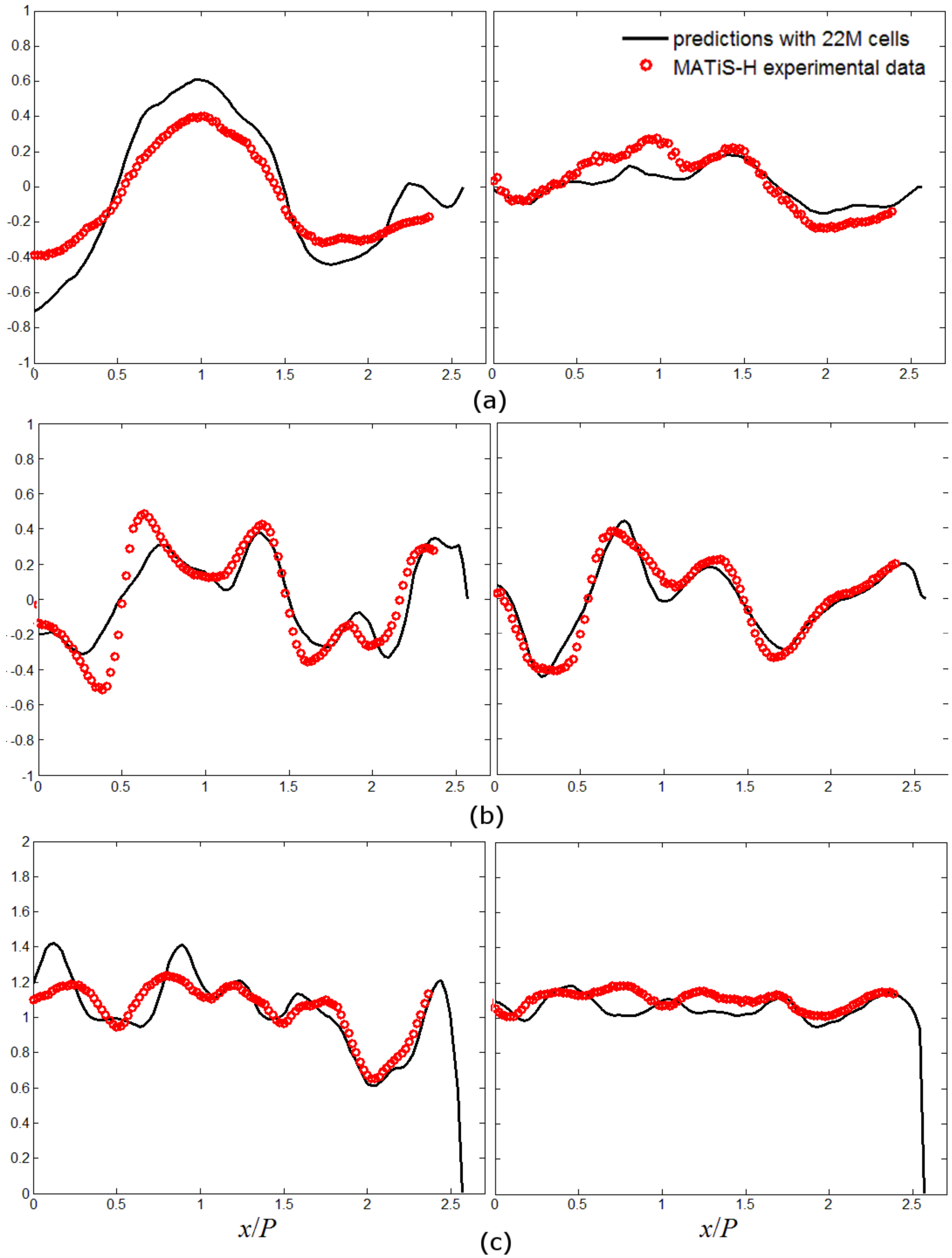

Figure 18. Dimensionless time-averaged velocity components at y = 0.5P; z = 1D_h (left column), z = 4D_h (right column); (a) spanwise velocity V_x/V_b, (b) transverse velocity V_y/V_b, (c) streamwise velocity V_z/V_b.

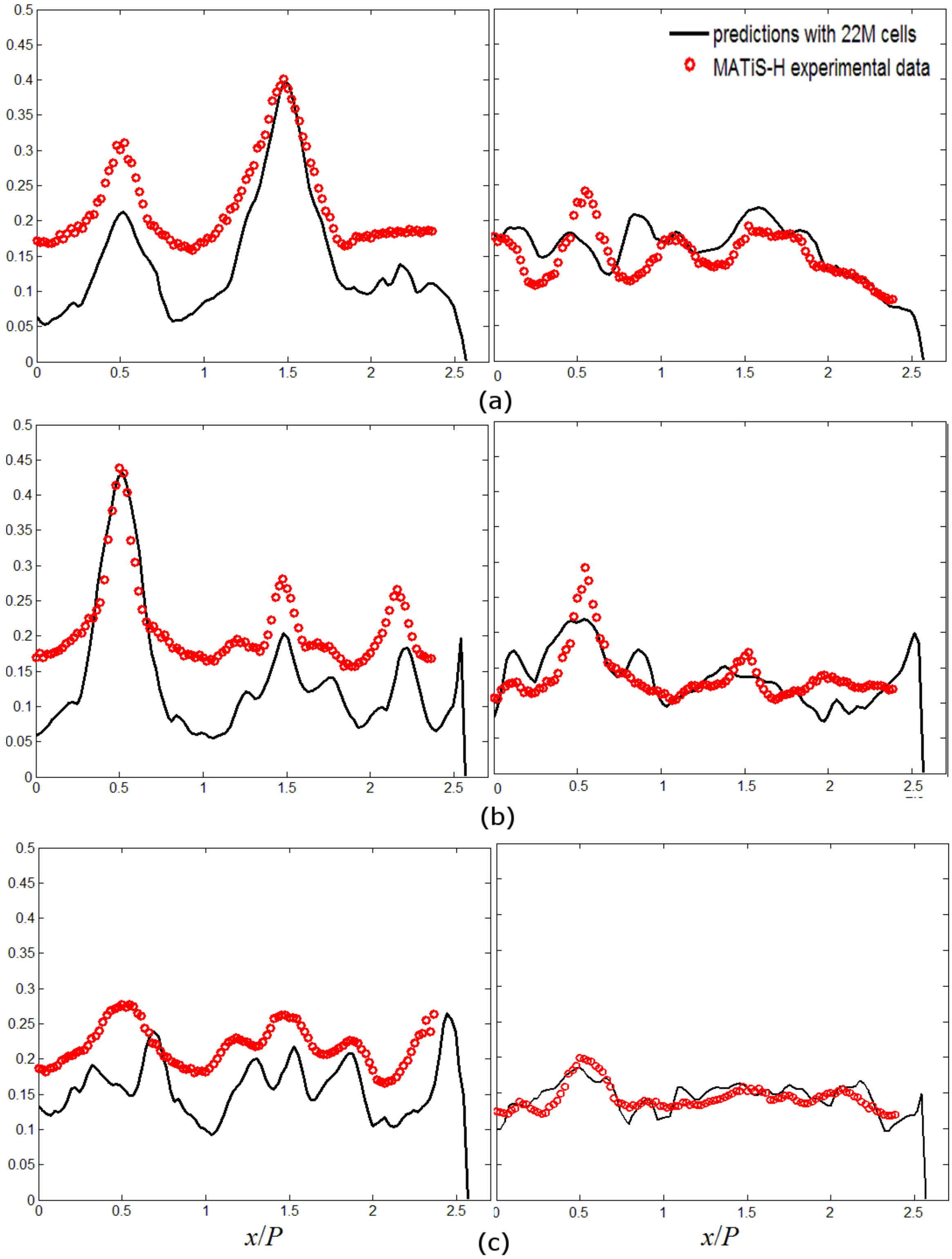

Figure 19. Dimensionless rms velocity fluctuations at $y = 0.5P$; $z = 1D_h$ (left column) and $z = 4D_h$ (right column); (a) rms spanwise fluctuations $V`_x/V_b$, (b) rms transverse fluctuations $V`_y/V_b$, (c) rms streamwise velocity fluctuations $V`_z/V_b$.

Figure 20 shows iso-contours of streamwise vorticity in a subchannel marked in Fig. 17 by a blue dashed box. In this subchannel, streamwise vorticity should be negative as a result of the orientations of the split-vane tips (OECD/NEA, 2012; Lee *et al*., 2012). The range of vorticity contours is from -350 to 350 s^{-1}. Blue colour corresponds to -350 s^{-1}, whereas red colour corresponds to 350 s^{-1}; the number of contour levels is 20. Both the predicted and measured vorticity contours show a streamwise decay of the vorticity. The predicted contour shapes were significantly different from those of the measured ones at $z = 0.5D_\mathrm{h}$ and $1.0D_\mathrm{h}$ and less so at $z = 4.0D_\mathrm{h}$ and $10.0D_\mathrm{h}$. The predicted contours indicated the presence of several small but strong vortical structures near the rods, whereas only some of these structures, but with much lower strengths, may be seen in some of the measured contours. It must be noted that the range of velocity measurements did not extend near the rod walls and as a result the vorticity near the walls could not be calculated from the measurements. In contrast, the predictions covered the entire flow area. Following the submission of the data, KAERI acknowledged this difference and suggested to the participants to exclude the annular regions indicated in Fig. 21 from the calculation of circulation, so that the computed and measured circulation values would be evaluated using the same area.

Figure 22 shows the streamwise variation of circulation. The plotted predictions are the revised ones, corresponding to the modified subchannel area shown in Fig. 21 and sent to KAERI on June 19, 2012. The predicted circulation matched the measured one at $z = 0.5D_\mathrm{h}$, but was lower than the latter at the three downstream measurement planes. Nevertheless, the trends of both the predicted and the measured simulations were similar, and both showed a negative peak magnitude at $z = 1.0D_\mathrm{h}$.

Streamwise location (z)	$0.5D_h$	$1.0D_h$	$4.0D_h$	$10.0D_h$
MATiS-H experiment (Lee *et al.*, 2012)	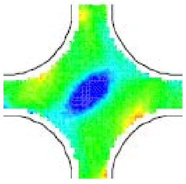	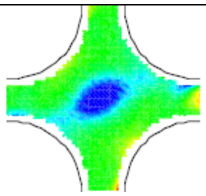	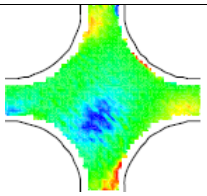	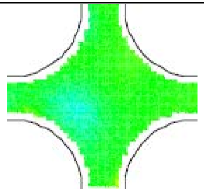
Hybrid simulation with 22M cells	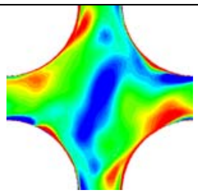	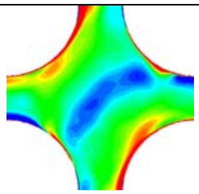	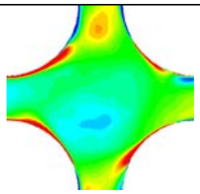	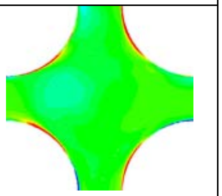

Figure 20. Iso-contours of streamwise vorticity in the range -350 s^{-1} < ω_z < 350 s^{-1}.

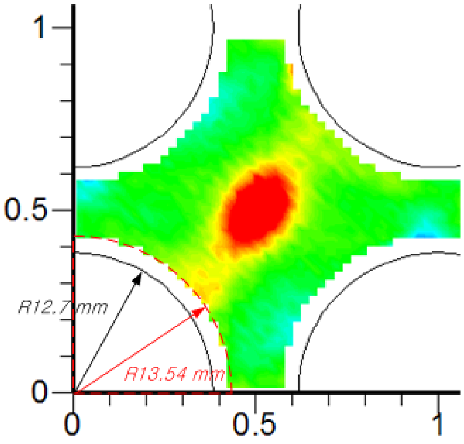

Figure 21. Representative iso-contours of the measured streamwise vorticity, showing the annular regions near the rod walls in which vorticity predictions were excluded from the calculation of circulation.

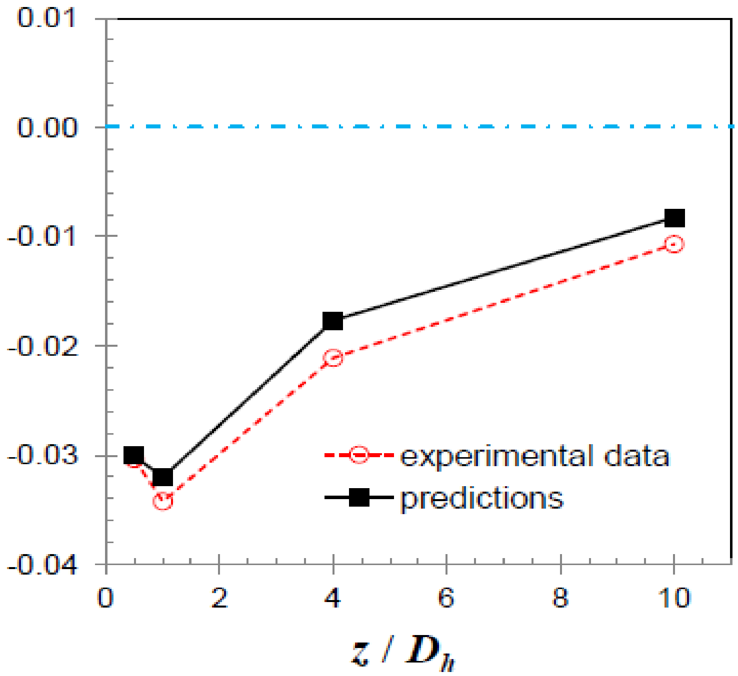

Figure 22. Streamwise variation of circulation (m^2/s).

5.2.2. Swirl-vane spacer grid simulations

KAERI received 14 submissions for the swirl-vane spacer grid case, including our submission with a mesh of 20M cells. The cell size was based on the mesh dependence analysis using RANS simulations. Our time-averaged velocity data at $z = 1.0D_h$ were ranked at number one, whereas our velocity data at $z = 4.0D_h$ were ranked at number four.

Figure 23 shows the time-averaged velocity profiles at $y = 0.5P$ for $z = 1.0D_h$ and $4.0D_h$. Unlike the split-vane case, the calculated time-averaged velocity shows excellent agreement with the experimental data. This indicates that the time-averaged velocity predictions were highly dependent on the mesh quality and not as much on the mesh size.

Figure 24 shows the rms velocity fluctuation profiles at $y = 0.5P$ for $z = 1.0D_h$ and $4.0D_h$. The simulations underpredicted the measurements, which is attributed to the mesh in the downstream rod bundle zone being too coarse to resolve the small-scale motions of turbulence.

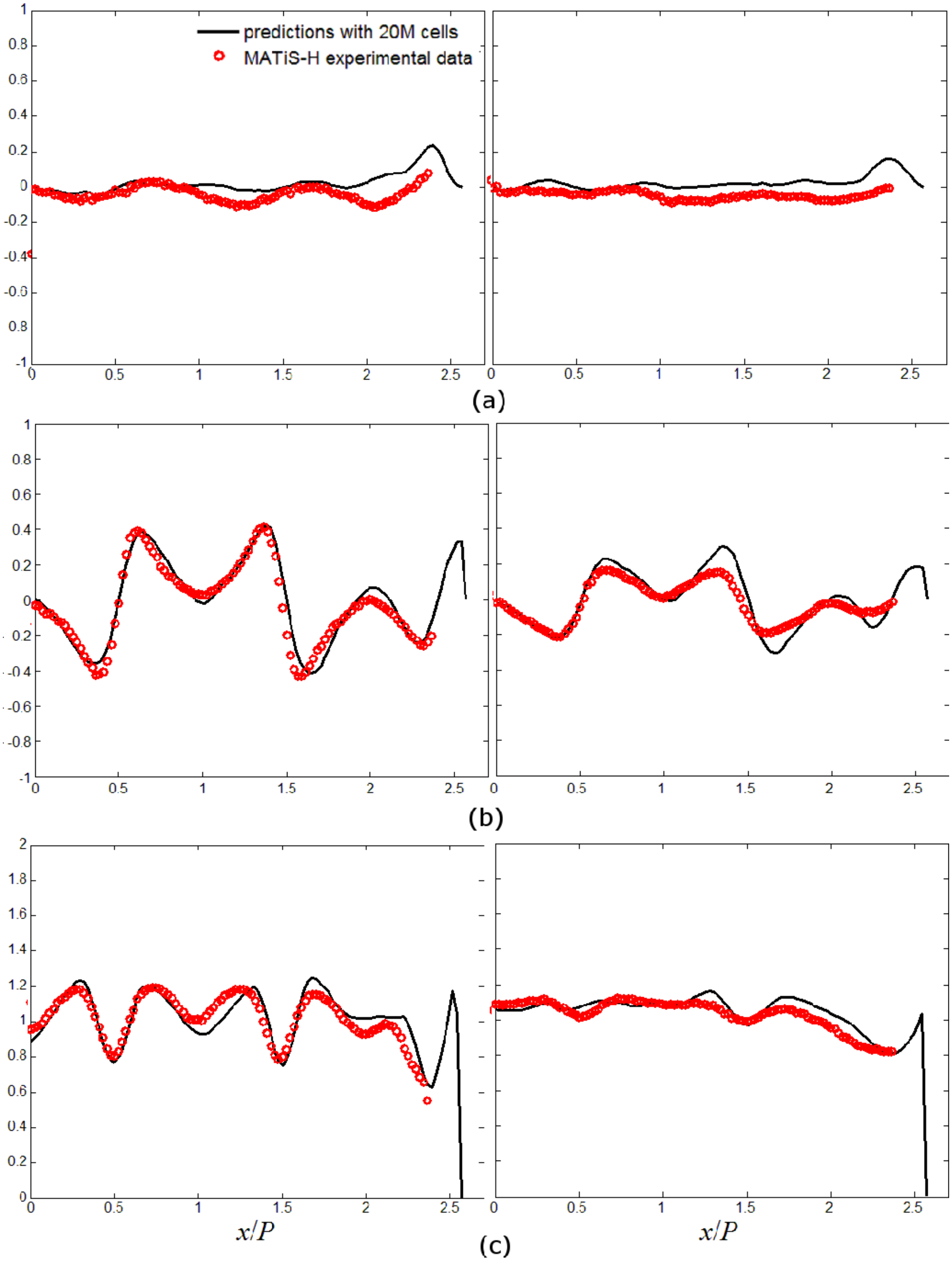

(a)

(b)

(c)

Figure 23. Dimensionless time-averaged velocity components at y = 0.5P; z = 1D_h (left column), z = 4D_h (right column); (a) spanwise velocity V_x/V_b, (b) transverse velocity V_y/V_b, (c) streamwise velocity V_z/V_b.

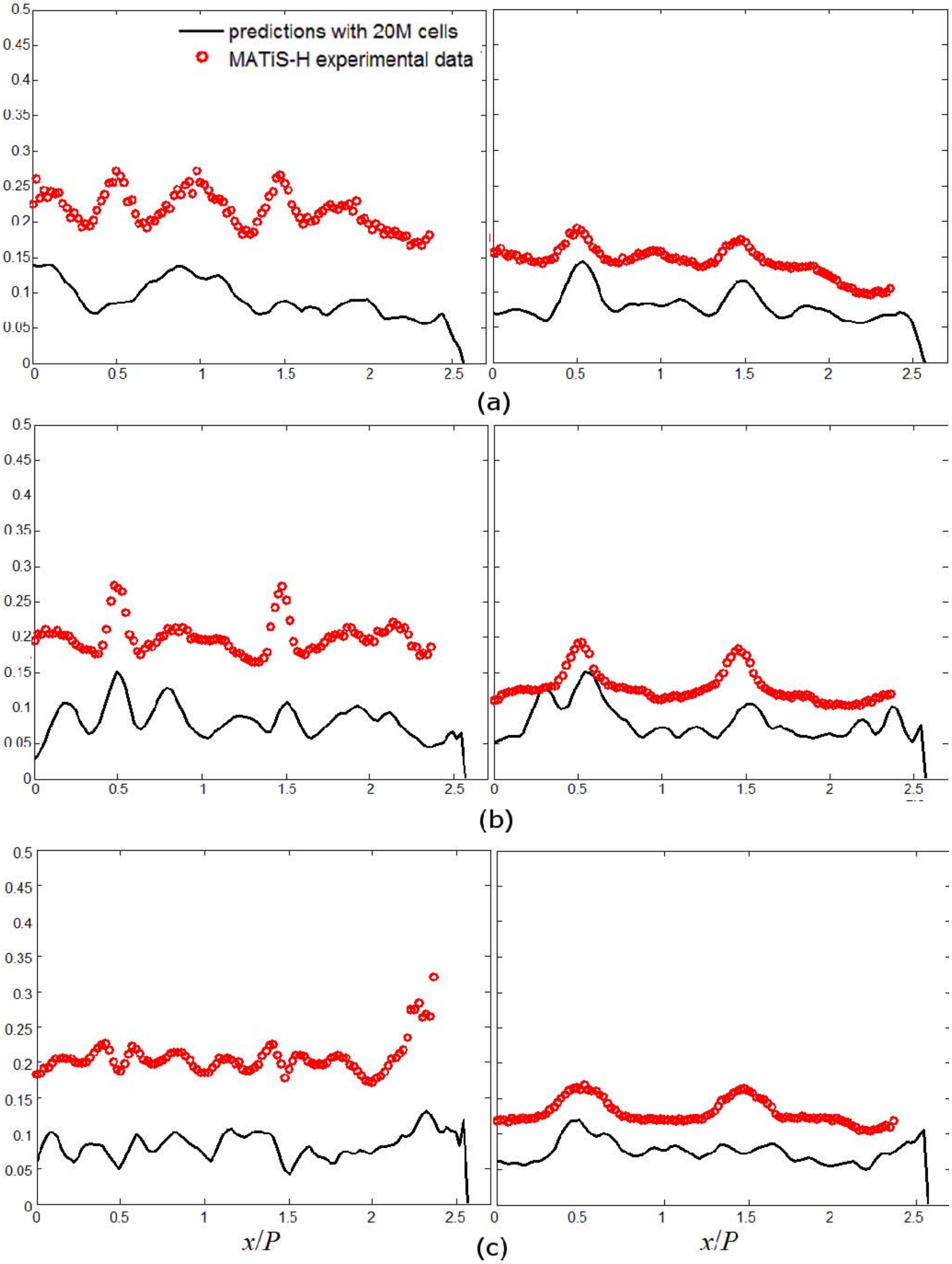

Figure 24. Dimensionless rms velocity fluctuations at $y = 0.5P$; $z = 1D_h$ (left column) and $z = 4D_h$ (right column); (a) rms spanwise fluctuation $V`_x/V_b$, (b) rms transverse fluctuation $V`_y/V_b$, (c) rms streamwise velocity fluctuation $V`_z/V_b$.

Figure 25 shows iso-contours of streamwise vorticity for the swirl-vane configuration. Unlike the split-vane configuration predictions (Fig. 20), the swirl-vane simulation reproduced fairly well the contour shapes of the measured streamwise vorticity in the open channel. Similarly to the split-vane predictions, vortical structures near the rods were also seen in the swirl-vane configuration.

Figure 26 shows the variation of circulation along the streamwise direction for the swirl-vane configuration. The predicted circulation values at $z = 0.5D_\mathrm{h}$ and $1.0D_\mathrm{h}$ differed from the measured data as the result of the strong predicted vortices near the rods. However, fair agreement between the measurements and the simulations were achieved at $z = 4.0D_\mathrm{h}$ and $10.0D_\mathrm{h}$.

Streamwise location (z)	$0.5D_\mathrm{h}$	$1.0D_\mathrm{h}$	$4.0D_\mathrm{h}$	$10.0D_\mathrm{h}$
MATiS-H experiment (Lee *et al.* ,2012)	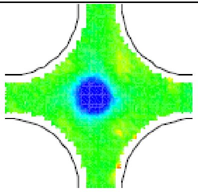	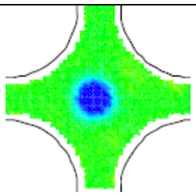	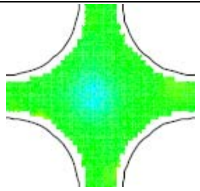	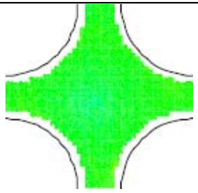
Hybrid simulation with 22M cells	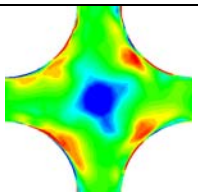	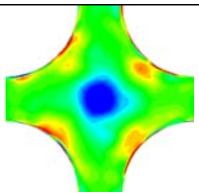	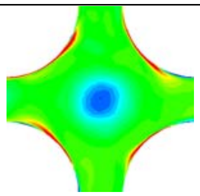	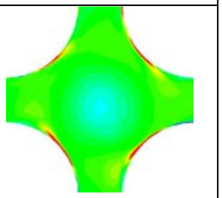

Figure 25. Iso-contours of streamwise vorticity in the range -350 $\mathrm{s}^{-1} < \omega_z <$ 350 s^{-1}.

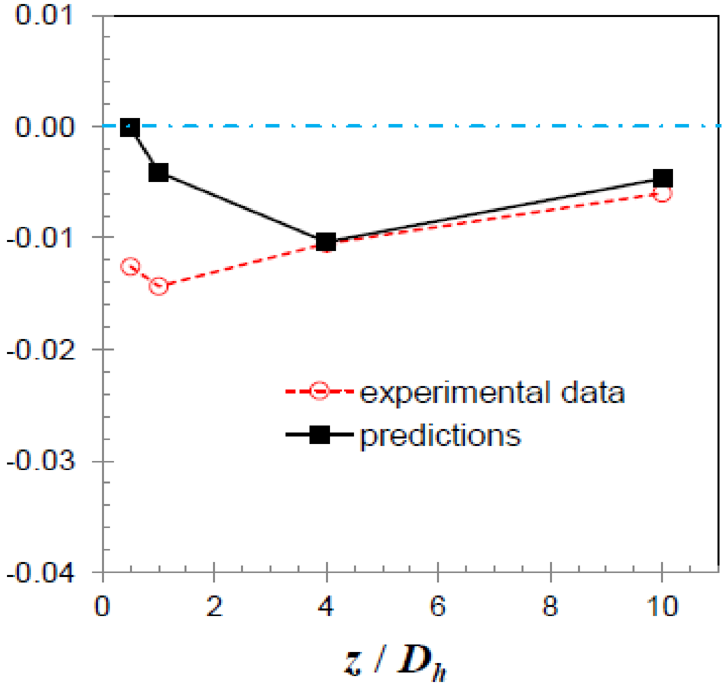

Figure 26. Streamwise variation of circulation (m^2/s).

6. Refined split-vane spacer grid simulation

The hybrid simulations with 40M cells for the split-vane case was run and presented in the poster session at the CFD4NRS-4 workshop (Chang and Tavoularis, 2012b).

Figure 27 shows the time-averaged velocity profiles at $y = 0.5P$ for $z = 1.0D_\mathrm{h}$ and $4.0D_\mathrm{h}$. Predictions show fair agreement with the experimental data.

Figure 28 shows the rms velocity fluctuation profiles at $y = 0.5P$ for $z = 1.0D_\mathrm{h}$ and $4.0D_\mathrm{h}$. Predictions of the turbulence stresses at $z = 1.0D_\mathrm{h}$ were very close to the measured data. At $z = 4.0D_\mathrm{h}$, however, differences between the profiles are visible, although the overall predicted turbulence levels were very similar to the measured ones.

Figure 29 shows iso-contours of streamwise vorticity for the refined simulation with the split-vane spacer grid. Predicted vorticity contours from the 22M case, presented previously in Fig. 20, are also shown for comparison. Compared to the 22M case, the 40M case shows better agreement with the measurements in the size and shape of vorticity contours in the open channel, especially at $z = 1.0D_\mathrm{h}$.

Figure 30 shows the variation of circulation along the streamwise direction for the two predictions with 22M cells and 40M cells, as well as the experimental data. Compared to the prediction with 22M cells, the refined simulation with 40M cells predicted better agreement at $z = 4.0D_\mathrm{h}$ but it had worse agreement at $z = 0.5D_\mathrm{h}$.

Overall, it can be concluded that the mesh refinement in the downstream rod bundle zone improved the agreement of the predictions with the measured data.

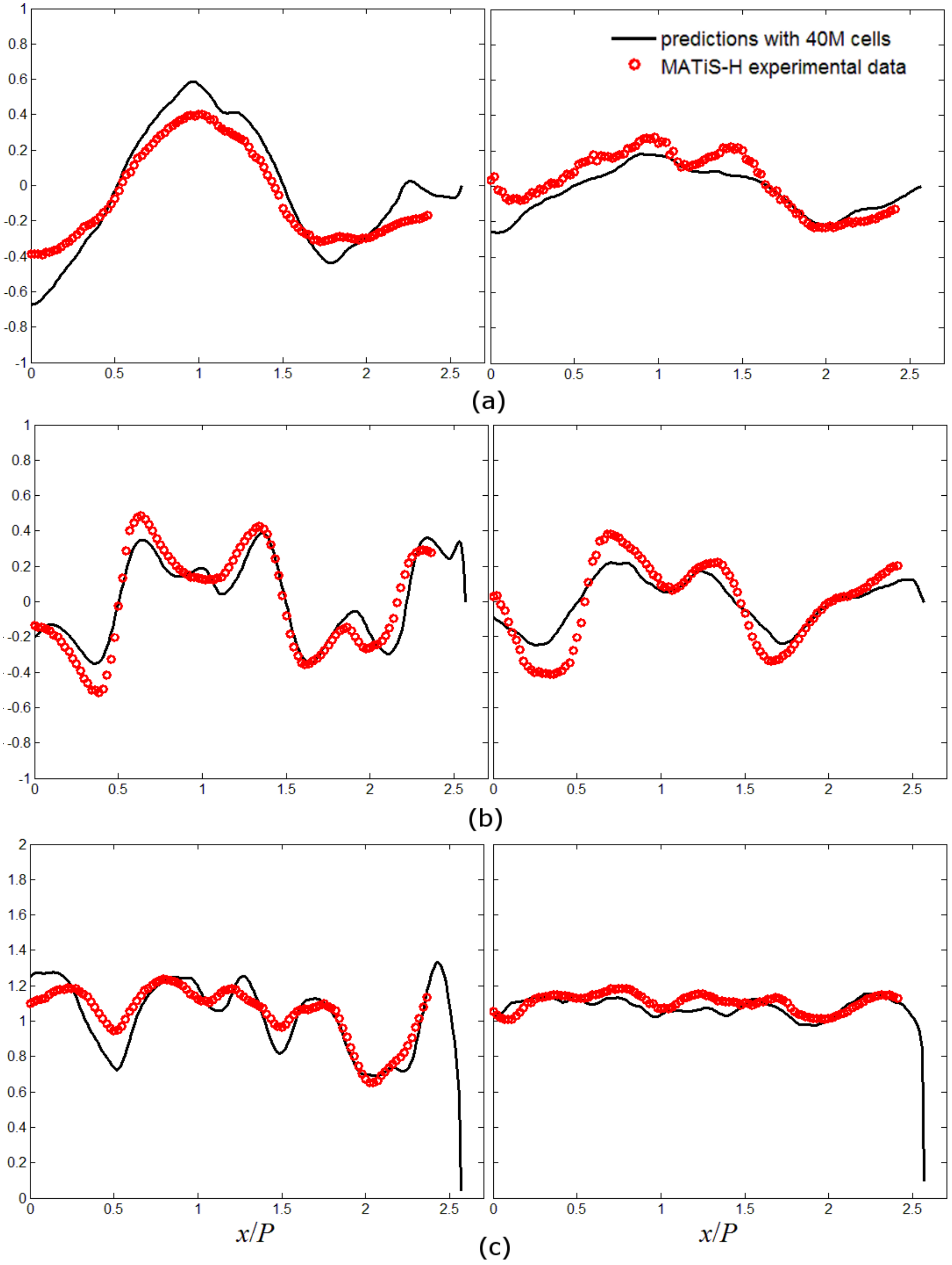

Figure 27. Dimensionless time-averaged velocity components at y = 0.5P; z = 1D_h (left column), z = 4D_h (right column); (a) spanwise velocity V_x/V_b, (b) transverse velocity V_y/V_b, (c) streamwise velocity V_z/V_b.

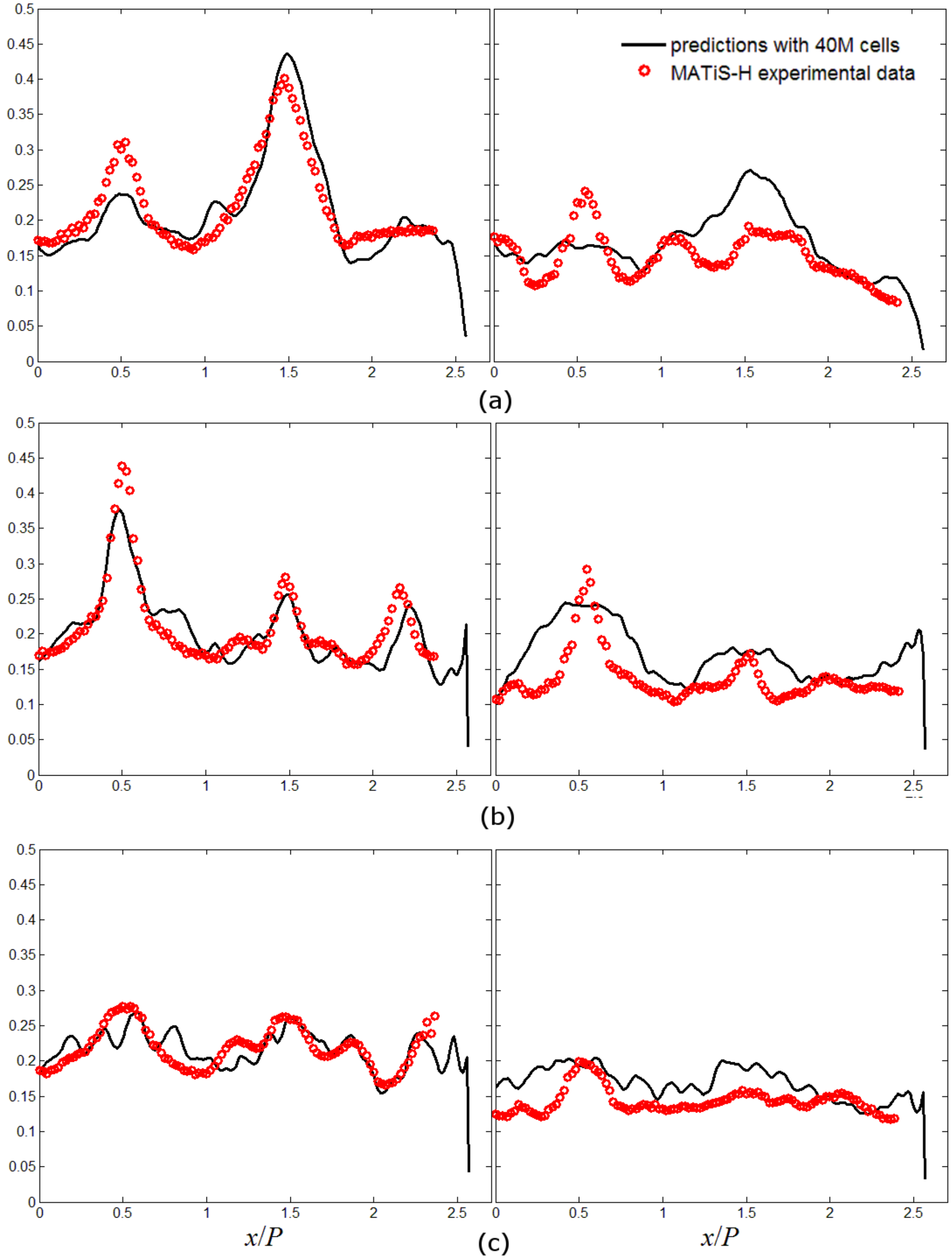

Figure 28. Dimensionless rms velocity fluctuations at $y = 0.5P$; $z = 1D_h$ (left column) and $z = 4D_h$ (right column); (a) rms spanwise fluctuation $V`_x/V_b$, (b) rms transverse fluctuation $V`_y/V_b$, (c) rms streamwise velocity fluctuation $V`_z/V_b$.

Streamwise location (z)	$0.5D_h$	$1.0D_h$	$4.0D_h$	$10.0D_h$
MATiS-H experiment (Lee *et al.* ,2012)	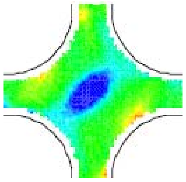	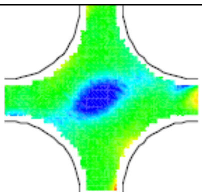	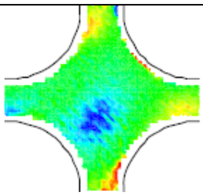	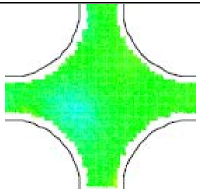
Hybrid simulation with 22M cells	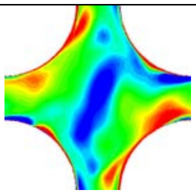	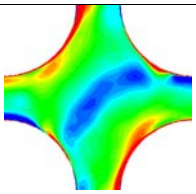	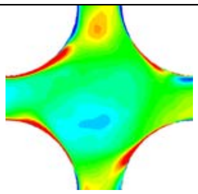	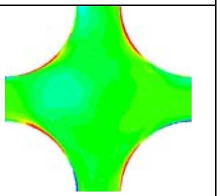
Hybrid simulation with 40M cells	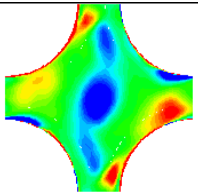	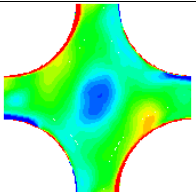	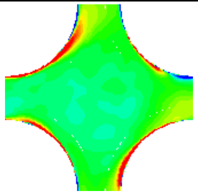	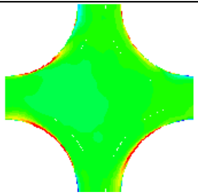

Figure 29. Iso-contours of streamwise vorticity in the range -350 s^{-1} < ω_z < 350 s^{-1}.

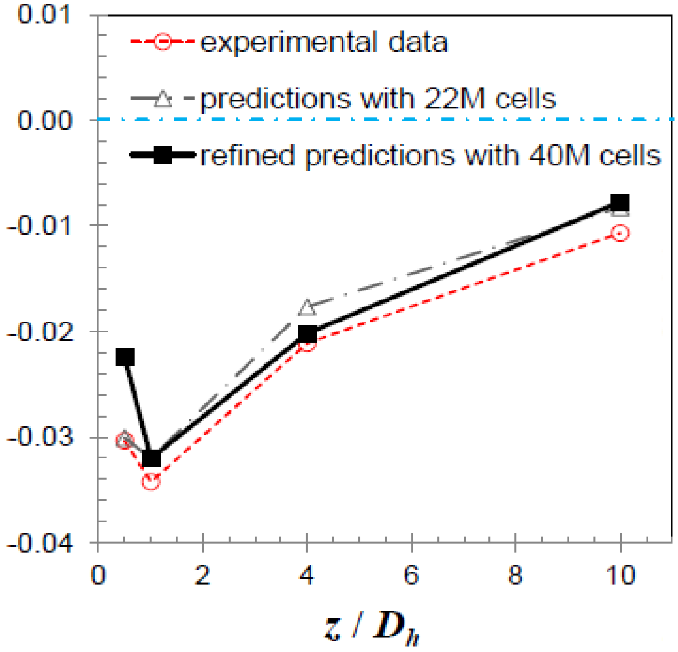

Figure 30. Streamwise variation of circulation (m^2/s).

7. Conclusion

Hybrid simulations for turbulent flows in the MATiS-H rod bundle with two types of vane spacer grids have been performed, as participation in the OECD/NEA-KAERI CFD benchmark exercise.

The two types of vane spacer grids were the split-vane spacer configuration and the swirl-vane spacer configuration. For the split-vane spacer configuration, although fair agreement was obtained between the predicted lateral velocity velocities and the experimental one, the predicted streamwise velocity was far from the measured one. This difference is attributed to the low mesh quality. For the swirl-vane spacer configuration, the predicted velocity shows excellent agreement with the experimental data. The predicted turbulence stress values for both spacer grid simulations were significantly lower than the experimental results. This is attributed to the mesh in the downstream rod bundle zone being too coarse. After refining the mesh in the downstream rod bundle zone, simulation results for the split-vane configuration were in good agreement with the experimental data. This indicates the importance of the mesh quality and mesh size, especially, in LES zones.

Acknowledgments

Financial support was provided by the Canadian Nuclear Safety Commission (CNSC). The authors would like to thank Mr. Jacek Szymanski of CNSC for his technical monitoring of this work and his valuable comments on this final report.

References

Chang, D.I. and Tavoularis, S., 2012a. Numerical Simulation of Developing Flow and Vortex Street in a Rectangular Channel with a Cylindrical Core, Nuclear Engineering and Design, vol.243, pp.176-199.

Chang, D.I. and Tavoularis, S., 2012b. Hybrid URANS/LES Simulations of Isothermal Water Flow in the MATiS-H Rod Bundle with a Split-Vane Spacer Grid, Poster Session, OECD/NEA & IAEA Workshop, Daejeon, Korea, Sept. 10-12.

Chang, S.K., Kim, S., Song, C-H., 2012. OECD/NEA-KAERI Rod Bundle CFD Benchmark Exercise Test, Proc. CFD4NRS-4, OECD/NEA & IAEA Workshop, Daejeon, Korea, Sept. 10-12.

Chapman, D., 1979. Computational Aerodynamics, Development and Outlook, AIAA journal, vol.17, pp.1293-1313.

Lee, J.R., Kim, J., Song, C-H., 2012. Synthesis of the OECD/NEA-KAERI Rod Bundle CFD Benchmark Exercise, Proc. CFD4NRS-4, OECD/NEA & IAEA Workshop, Daejeon, Korea, Sept. 10-12.

Menter, F.R., 1991. Influence of Freestream Values on k-ω Turbulence Model Predictions, AIAA Journal, vol.30, pp.1657-1659.

Menter, F.R., Egorov, Y., 2005. A Scale-Adaptive Simulation Model using Two-Equation Models, 43th Aerospace Science Meeting and Exhibit, AIAA paper 2005-1095, Reno, NV, USA.

Meyer, I., 2010. From Discovery to Recognition of Periodic Large Scale Vortices in Rod bundles as Source of Natural Mixing between Subchannels – a Review, Nuclear Engineering and Design, vol.240, pp.1575-1588.

Nicoud, F. and Ducros, F., 1999. Subgrid-Scale Stress Modelling based on the Square of the Velocity Gradient Tensor Flow, Turbulence and Combustion, vol.62, pp.183–200.

OECD/NEA, 2012. MATiS-H Benchmark – Final Benchmark Specification, 2012.

Sergent, M.E., 2002. Vers une Méthodologie de Couplage Entre la Simulation des Grandes Echelles et les Modèles Statistiques, Phd Thesis, Ecole Cetnral de Lyon.

Szymanski, J., Chang, D.I., Novog, D., Podila, K., Bailey, J., Rao, Y., Rashkovan, A., and Tavoularis, S., 2012. Canadian Participation in OECD/NEA-KAERI Rod Bundle Benchmark for CFD Codes, 24th Nuclear Simulation Symposium, Ottawa, Canada, October 14-16.

Tavoularis, S., 2011. Rod Bundle Vortex Networks, Gap Vortex Streets, and Gap Instability: a Nomenclature and Some Comments on Available Methodologies, Nuclear Engineering and Design, vol.241, pp.2624-2626.

Wornom, S., Ouvrard, H., Salvetti, M.V., Koobus, B., and Dervieux, A., 2011. Variational Multiscale Large-Eddy simulations of the Flow Past a Circular Cylinder: Reynolds Number Effects, Computers and Fluids, vol.47, pp.44-50.

Yakhot, V. and Orszag, S.A., 1986. Renormalization Group Analysis of Turbulence: I. Basic Theory, Journal of Scientific Computing, vol.1, pp.3-51.